Journal of Molecular Liquids 370 (2023) 121002

Contents lists available at ScienceDirect

Journal of Molecular Liquids

journal homepage: www.elsevier.com/locate/molliq

Protein-stabilized bimetallic Au/Ag nanoclusters as fluorescent reporters: Synthesis, characterization and their interactions with biocolloids

Árpád Turcsányi [a,b], Ditta Ungor [a], Marek Wojnicki [c], Edit Csapó [a,b,*]

[a] MTA-SZTE Lendület "Momentum" Noble Metal Nanostructures Research Group, University of Szeged, H-6720, Rerrich B. sqr. 1, Szeged, Hungary
[b] Interdisciplinary Excellence Center, Department of Physical Chemistry and Materials Science, University of Szeged, H-6720 Rerrich B. sqr. 1, Szeged, Hungary
[c] AGH University of Science and Technology, Faculty of Non-Ferrous Metals, Mickiewicza Ave, 30, 30-059 Krakow, Poland

ARTICLE INFO

Article history:
Received 21 October 2022
Revised 30 November 2022
Accepted 3 December 2022
Available online 9 December 2022

Keywords:
Bimetallic nanoclusters
Gold-silver
Fluorescence
Drug carrier particles
Biolabeling

ABSTRACT

Fabrication protocol of bovine serum albumin-(BSA) and lysozyme-(LYZ) stabilized gold/silver bimetallic nanoclusters (Au/Ag NCs) have been reported via optimization of the protein/metal ion ratios, metal concentration, pH and incubation time. No other reducing and stabilizing compounds were used to produce these nanoclusters at room temperature. Incorporation of small quantities of silver (~3–10 w%) into the gold core substantially changed the optical features such as the enhancing of the quantum yield and blue shifting of the emission wavelength compared to their purely gold-based derivatives. Applicability of the BSA- and LYZ-directed Au/Ag NCs having intense fluorescence at above ~ 600 nm as potential fluorescent reporters (FRs) has been studied by examining their interactions with chitosan/hyaluronic acid (Chit/HyA)-based colloidal drug delivery particles. It was found that, in contrast to the monometallic derivatives, our bimetallic NCs, prepared at room temperature and stabilized with larger amounts of proteins, exhibit a much higher degree of stability during interaction with biocolloids. The results are confirmed by fluorescence measurements in addition to light scattering studies, since the aggregation-induced emission is not observed dominantly, as clearly confirmed for Au-based NCs. Utilizing the alloying process and the milder preparation conditions can be a promising route to the synthesis of noble metal NCs-based FRs in biomedical field.

1. Introduction

The design of novel colloidal drug carrier particles has received increasing research support over the past decade [1]. Their use allows faster and more targeted delivery of the drug to the right site in the human body and a more controlled drug release can also be achieved [2]. Studying a new composite system makes testing and evaluation much easier if the route of the active substance, and therefore the composite can be traced in the body, mainly by labeling individual particles or complexes. Labeling of different tissues and cells is a well-known technique in medical science [3]. This method utilizes different markers for visualization of living/dead or cancer cells, and specific tissues. Among these methods, fluorescent labeling is promising, as it is easily visualized, and neither requires nor emits harmful radiation. However, fluorescent labeling is rarely used for drug carrier labeling, even though the path of carriers through the body could be traced, and targeted release could be visualized. Radioactive isotopes [4] are often used as a marking method, but fluorescent dyes like fluorescein, trypan blue, Hoechst stains, 4′,6-Diamidine-2′-phenylindole dihydrochloride (DAPI), propidium iodide [5], quantum dots [6] or gold nanorods [7] are also preferred for mainly cell imaging. As an alternative, noble metal nanoclusters (MeNCs) can be applied [8] because they possess adequate fluorescence intensity, which can be enhanced and optimized for desired applications. Different fluorescence emissions can be obtained by varying the size of the clusters, and hence the number of atoms that build up the clusters or the type of the stabilizing ligands [9]. MeNCs introduce no hazardous heavy metals like cadmium (Cd) for quantum dots [10] and by smart design (using biomolecules as stabilizers), they can be made biocompatible. The bimetallic nanoparticles (NPs) having sizes>2 nm, often show better optical and catalytic properties than their monometallic counterparts [11], so the fabrication of sub-nanometer sized bimetallic NCs having the structure- and composition-dependent tunable photoluminescence (PL) is the

* Corresponding author.
E-mail address: juhaszne.csapo.edit@med.u-szeged.hu (E. Csapó).

https://doi.org/10.1016/j.molliq.2022.121002
0167-7322/

extreme focus of interest. In the last *ca.* six years several new NCs have been synthesized by our group using template-assisted synthesis, where proteins, peptides, amino acids, or nucleotides have been applied as reducing and stabilizing agents [12–15], *etc*. Here, we mainly focus on the protein-stabilized NCs using exclusively BSA and LYZ. For BSA-stabilized NCs, several compositions have been fabricated since 2010, such as Zn/Cu [16], Au/Cd [17], Au/Pt [18], Au/Cu or Au/Ag [19–26]. For the latter case, in almost all publications either an extra reducing agent ($NaBH_4$ or ultrasonic treatment) is used or the synthesis is carried out at higher (37 °C or ~ 80 °C) temperatures. For LYZ, only two articles were published for synthesis of Au/Ag [27] and Au/Mo [28] NCs, thus the design of new synthetic routes is highly justified.

Based on these findings, our aim was the optimization of new preparation protocols for Au/Ag NCs reduced and stabilized only with BSA and LYZ at room temperature, and without the application of extra reducing agents. Exploiting their advantegous optical properties and excellent stability thanks to the alloying process, we studied their potential application as fluorescent labelling agents for drug delivery monitoring, because in the literature these NCs are dominantly used for cell and tissues imaging. Interactions of these alloy NCs with drug carrier biocolloids have been studied focusing on the colloidal and optical properties of such systems, because the knowledge of these parameters is essential and primary information to design suitable systems.

2. Materials and methods

2.1. Materials

Bovine serum albumin (BSA, ≥ 98 %, heat shock fraction, protease, fatty acid and essentially globulin free, Sigma, USA), lysozyme (LYZ, ≥ 90 %, from chicken egg white, Sigma, Canada), hydrogen tetrachloroaurate ($HAuCl_4 \cdot 3H_2O$, 99.9 % (metal basis), Alfa Aesar, Germany), silver nitrate ($AgNO_3$, > 99.9 %, Molar Chemicals, Hungary), Sodium hydroxide (NaOH, > 99.0 % Molar Chemicals, Hungary). Hydrochloric acid (HCl, 33 w% solution, Molar Chemicals, Hungary), sodium chloride (NaCl, Molar Chemicals, Hungary), chitosan (high molecular weight, 310 – 375 kDa, > 75 % deacetylated, Sigma, Iceland), hyaluronic acid sodium salt (from *Streptococcus equi*, 1.5–1.8 × 10^6 Da, ≤ 1% protein, Sigma, Czech Republic), pentasodium triphosphate (tripolyphosphate, TPP, for BOD determination, Merck GmbH, Germany), acetic acid (>95 vol%, Erdőkémia, Hungary). Highly purified Milli-Q water was obtained by deionization and filtration with a Millipore purification apparatus (18.2 MΩ·cm at 25 °C). All chemicals were used without further purification.

2.2. Preparation of protein-stabilized bimetallic gold-silver nanoclusters

2.2.1. BSA-stabilized Au/Ag NCs

45 mg of BSA was dissolved in 5.0 mL MilliQ water, then stirred for 15 min for complete dissolution. The metal salts were then added to the protein solution in the following order: first, 230 μL of 10 mM $HAuCl_4$ (0.453 mg total gold content per sample) and 25 μL of 10 mM $AgNO_3$ solution (0.027 mg total silver content) were added and left for stirring for five minutes. The solution color changed from yellow (initial aurate) to orange, then faded to a pale yellow color. After ensuring sufficient time for the formation of complexes, the pH was adjusted to pH ~ 12 by using a 1.0 M NaOH solution. The color of the sample turned to stronger yellow, which remained during the whole process. The reduction period was carried out without stirring, protected from sunlight at room temperature (~20–25 °C) for 16 h. In the final product (before purification) BSA:Au:Ag 100:1.0:0.06 wt ratio (Au: 95 w%, Ag: 5 w%) was obtained.

2.2.2. LYZ-stabilized Au/Ag NCs

Two dispersions (LYZ_I-Au/Ag and LYZ_{II}-Au/Ag NCs) were synthesized having orange-red and yellow emissions, respectively. Namely, 45 mg (LYZ_I-Au/Ag) or 60 mg (LYZ_{II}-Au/Ag) LYZ was dissolved in MilliQ water and the solution was stirred for 15 mins. As a second step, appropriate amounts of metal precursors were also added as 217.5 μL or 180 μL 10 mM $HAuCl_4$ (0.428 mg or 0.355 mg total gold content), and 37.5 μL or 11.3 μL 10 mM $AgNO_3$ solution (0.040 mg or 0.012 mg total silver content), respectively. After adding the metal salts, the sample color quickly changes from yellow to orange, then into a pale-yellow color. After 5 min stirring, the pH was adjusted to pH ~ 12 by using a 1.0 M NaOH solution. The samples were left for NC formation without stirring and protected from light at room temperature for 24 h. In the final product (before purification) LYZ_I:Au:Ag 100:1.0:0.09 (Au: 92 w%, Ag: 8 w %) and LYZ_{II}:Au:Ag 125:1.0:0.03 (Au: 97 w%, Ag: 3 w%) weight ratios were obtained.

The prepared samples were purified by dialysis using a 14 kDa molecular weight cut-off cellulose membrane in all cases. After purification, the distribution of the metals was slightly changed, as shown in **Table S1**. To compare the structural and optical properties of these NCs the BSA-Au NCs and LYZ-Au NCs were also prepared by using our preparation protocols described in our previous papers [29–31].

2.3. Preparation of polysaccharide-based biocolloids

The qualification of the bimetallic NCs for fluorescent labeling was investigated with previously prepared and well-characterized polysaccharide-based colloidal particles [32]. The description of the biocolloids is summarized in Supplementary (**Scheme S1**).

2.4. Design of carrier particles labeled with fluorescent NCs

The labeling experiments - using the cleaned bimetallic NCs synthesized at the optimized experimental conditions - were performed based on our previously described method [33].

2.5. Characterization methods

2.5.1. Dynamic light scattering and zeta potential

The aggregation tendency (change of the size) of the alloy NCs and the Zeta potential values of the NCs-labelled biocolloids were investigated in the range of pH = 1–12 (I = 0.10 M (NaCl)) by using Horiba SZ-100 NanoPartica nanoparticle analyzer equipment. The device was equipped with a diode-pumped Nd:YAG laser possessing a 532 nm emission wavelength.

2.5.2. ICP-MS and XPS

To perform inductively coupled plasma mass spectrometry (ICP-MS) studies the dispersions were dissolved in hot aqua regia using 1 h contact time and the solutions were diluted by ultrapure water. Multipoint, matrix-matched calibration was applied by IV-ICPMS-71C certified calibration standard (Inorganic Ventures), while the plasma and interface parameters were optimized by standard tuning solutions (G1820-60410, Agilent). The data processing was accomplished within the Agilent Mass Hunter software. The X-ray photoelectron spectroscopy (XPS) measurements were carried out on a SPECS instrument equipped with a PHOIBOS 150MCD9 hemispherical analyzer. For the analyzer transmission mode, 40 eV pass energy was selected, while the high-resolution scan was carried out with 20 eV pass energy. The sample was

deposited by multistep cyclic freeze drying on a titanium foil having 0.5 mm thickness (Sigma). The Al K_α X-ray source was used at 200 W power. The 4f peak of the platinum substrate (71.00 eV) was used for charge referencing and the registered spectra were evaluated by CasaXPS software.

2.5.3. CD and FT-IR

The circular dichroism (CD) spectra were recorded on a JASCO J-1100 spectrometer between 190 and 300 nm with 1 cm optical length at room temperature. The percentage of the secondary structure elements was calculated by the Reed model [34] with the JASCO SpectraManager 2.0 Secondary Structure Estimation program. The Fourier-transformed Infrared spectroscopy (FT-IR) spectra were recorded on a JASCO FT/IR-4700, which was equipped with an ATR PRO ONE Single-reflection accessory. The IR spectra were registered in the range of 500 to 4000 cm^{-1} with 1 cm^{-1} resolution and 128 interferograms. The measurements were conducted on the lyophilized protein-NCs and the lyophilized protein powders after the dissolution of the BSA and LYZ at the same concentrations and similar pH to the cluster dispersions.

2.5.4. Spectrofluorimetry

The fluorescence spectra were recorded on the JASCO FP-8500 fluorimeter with a Xe lamp light source. The measurements were done using λ_{ex} = 365 (BSA) and 370 nm (LYZ) excitation wavelengths with 2.5–2.5 nm slit values, 1 nm resolution, and 200 nm/min scan speed in a 1 cm quartz cuvette. The absolute internal quantum yield (QY) was calculated by the incident light, and direct and indirect excitation spectra of the samples, which were registered on the same instrument with the JASCO ILF-835 integrating sphere (d = 100 mm). For the calibration of the instrument, the JASCO ESC-842 calibrated WI lamp was applied, while further references for the calculations were not necessary. The fluorescence lifetime (τ) of the samples was measured by time-correlated single photon counting technique (TCSPC) on a Horiba DeltaFlex fluorometer equipped with a DeltaDiode pulsed laser light source (λ_{laser} = 371 nm). The emitted light was detected at λ_{em} = 630 nm, 610 nm and 580 nm in the case of BSA-Au/Ag, LYZ_I-, and LYZ_{II}-Au/Ag, respectively. During the measurements, a 6 nm slit was selected and the number of counts on the peak channel was 2500 due to the long lifetime components. To determine the instrument response function (IRF), the SiO_2 colloid dispersion was applied and manufactured by Horiba. The main lifetime components were calculated by the exponential fitting of decay curves and the goodness of fitting was characterized by χ^2 values.

2.5.5. Fluorescence microscopy

For microscopic studies, the applicability of the BSA-Au/Ag NCs and the LYZ_I-Au/Ag NCs as labeling agents were studied. The effectiveness of the labeling procedure was investigated using a Leica confocal fluorescence microscope. The labeled drug carriers were dried on a glass slide using a similar process as described previously [33]. The dried samples were analyzed under visible light, and also with UV-light irradiation using a red filter.

3. Results and discussion

3.1. Optimization of the production of protein-stabilized bimetallic NCs

3.1.1. BSA-stabilized Au/Ag NCs

To optimize the preparation process of the BSA-Au/Ag NCs, for the first experiment, the interaction of BSA with metal ions ($[AuCl_4]^-/Ag^+$) have been studied at 40 °C at pH ~ 12. *The ratio of the metal ions* was changed in a way that a certain amount of $[AuCl_4]^-$ was exchanged for an equal amount of Ag^+ and thus $[AuCl_4]^-/Ag^+$ molar ratios were tuned. The ratio of the protein to metal ions (15 mg protein/1.0 mmol metal ions) was constant. After 24 h, the characteristic PL emission maximum is detected at $\lambda_{BSA\text{-}Au\ NCs}$ = 660 nm [30,31] and it was found that the increase in the Ag weight content from ~ 5 w% to *ca.* 15 w% results in the shift of the emission maxima to ~ 630–640 nm which is confirmed by the change of the colors of the samples under UV lamp. With further increase in the Ag content, the emission maximum is observed at ~ 730 nm with low intensity and the presence of Ag NPs is also confirmed which is supported by the brownish yellow color of the dispersion. Based on these findings the sample with the highest fluorescence intensity ($Au_{95w\%}/Ag_{5w\%}$, λ = 640 nm) was chosen for further experiments.

In the next step, *the effect of protein concentration* was examined by changing the value from 1 mg to 150 mg (BSA:Au:Ag 1.0:1.0:0.06–270:1.0:0.06 wt ratio) in each sample, while the 95:5 Au/Ag w% was kept constant. For low BSA content, the colors were different shades of purple, indicating the formation of plasmonic Au or Au/Ag alloy NPs. When BSA excess reached the BSA:Au:Ag 18:1.0:0.06 the color changed to yellow, which refers to the presence of smaller Au/Ag nanoobjects with characteristic PL. As Fig. 1A shows the PL intensity continuously increases to BSA:Au:Ag 100:1.0:0.06 wt ratio but at higher ratio, the intensity starts to decrease. For this reason, this weight ratio having maximum PL intensity was chosen for further studies.

It is well-known that temperature also influences the formation of nano-objects [1,17], thus *the effect of temperature* was also studied. As Fig. 1B represents, temperatures higher than 40 °C are not favorable to cluster formation, presumably due to protein denaturation. At 80 °C, no red-emitting species could be observed. In contrast, when the synthesis is carried out at room temperature (25 °C), *ca.* 50 % more intensity can be detected than at 40 °C, but at 10 °C similar results were obtained. Based on these findings the room temperature was chosen as optimal value. By tuning the temperature, the PL emission maximum further shifted to λ = 612 nm.

After temperature optimization, *the effect of metal concentration* was investigated ranging from 0.30 to 5.63 times the amount of the original sample ($c_{original}$ = 1.0 mM). The sample color changed based on metal content: higher values resulted in more intensive, while lower values gave a lighter yellow color. The registered PL spectra indicated that the highest emission was detected at c_{metal} = 0.50 mM. Most probably the higher metal concentration is favourable to form plasmonic particles instead of clusters.

The *effect of reaction time* on the fluorescence was also investigated by continuously measuring the fluorescence spectra in given time intervals. In the first few hours, the spectra were recorded every 15 min, then 30 min, and hourly until 12 h. New samples were prepared to check the fluorescence after 16 h, which were aligned with the initial 24 h measurement. It was obtained that after 16 h the PL intensity started to decrease therefore the reaction time of 16 h was chosen instead of 24 h.

3.1.2. LYZ_I - and LYZ_{II}-Au/Ag NCs

In the case of LYZ-stabilized NCs same optimization pattern was followed as for BSA. In this case, only the initial protein content was changed to 20 mg as starting concentration. In the case of *gold:silver mass ratio*, the addition of a small amount of silver tremendously changed the fluorescence of the clusters from 660 nm to 580–620 nm depending on Ag content (1.5 – 10 w%) as Fig. 2A shows. In the investigated region two compositions were selected for detailed studies which showed higher intensity values compared to all samples. These two samples also possessed different emission maxima: for LYZ_{II}-Au/Ag NCs, the $\lambda_{em,max}$ appeared at 598 nm (*ca.* 3 w% Ag) and for LYZ_I-Au/Ag it was at λ^{max} = 629 nm (*ca.* 8 w% Ag). While both clusters had very promising characteris-

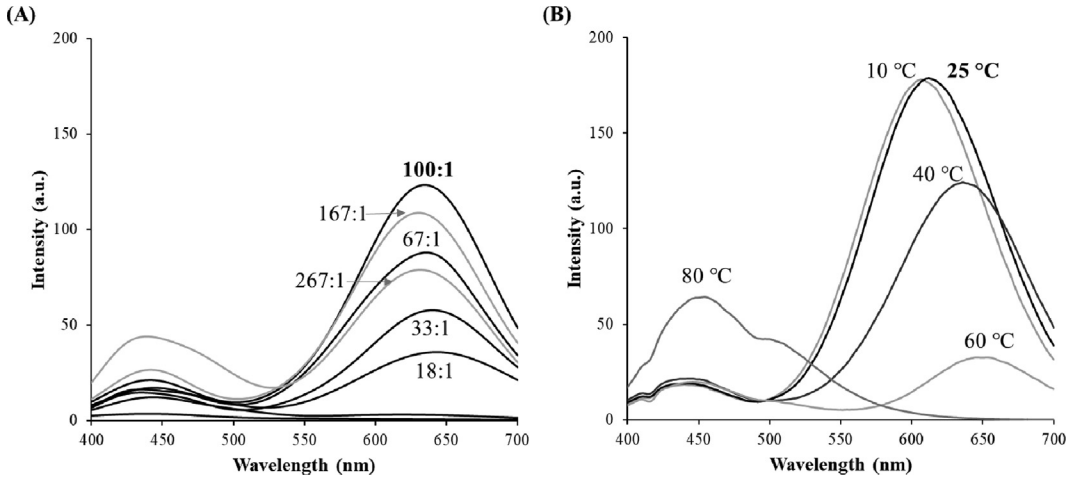

Fig. 1. PL emission spectra of BSA-stabilized Au/Ag NCs at different BSA:Au weight ratios at 40 °C (**A**) and PL spectra of the BSA-Au/Ag NCs using BSA:Au 100:1 wt ratio at various temperature values (**B**). λ_{ex} = 365 nm, c_{metal} = 1.0 mM, Au:Ag 95:5 w%.

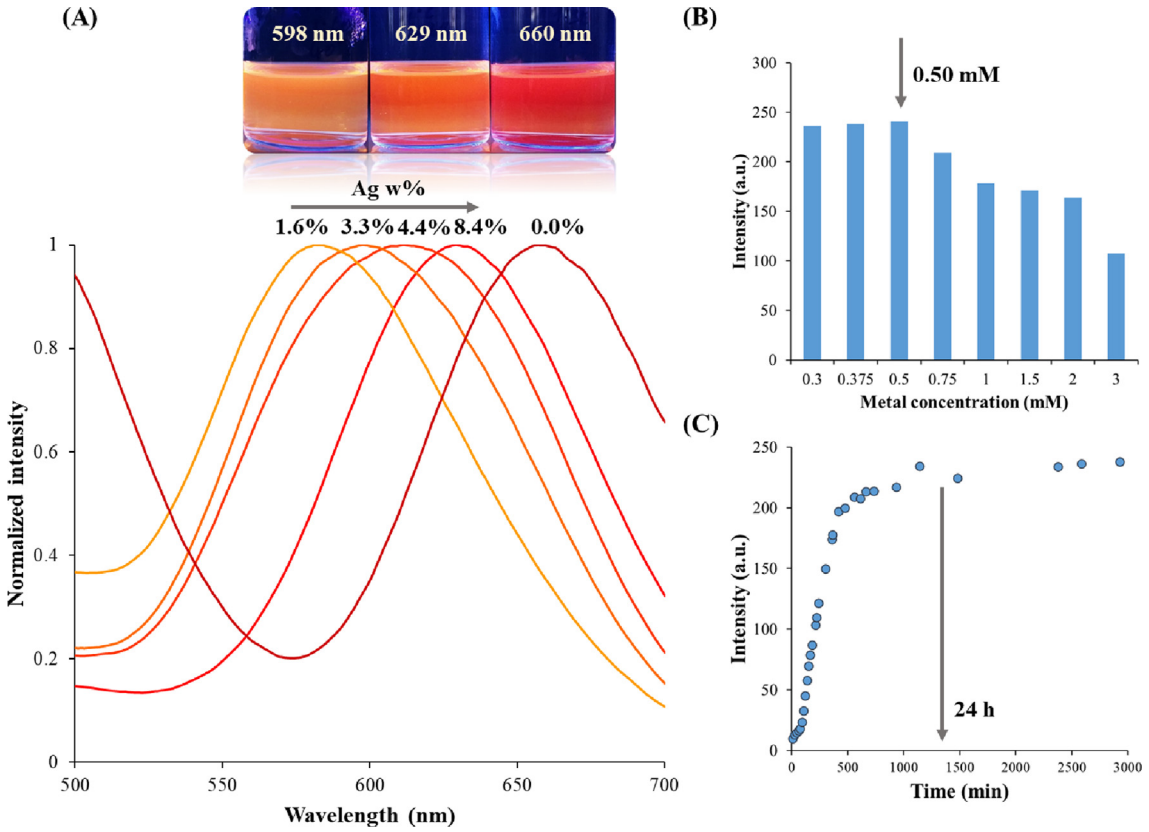

Fig. 2. Normalized PL emission spectra of LYZ-stabilized Au/Ag NCs at different Ag w% with the photos of some samples under UV lamp (λ_{ex} = 370 nm) (**A**) PL intensities of LYZ_{II}-Au/Ag NCs as a function of metal concentration (**B**) and time (**C**) (λ_{em} = 598 nm).

tics, the further optimization steps were performed in both cases. It was also found that below 1 w% Ag content two characteristic emission bands were detected at 660 nm and 570–575 nm referring to the presence of LYZ-stabilized pure Au NCs and Au/Ag alloy NCs as well. When the Ag content exceeds the *ca.* 1 w% the PL emission maximum of pure Au NCs disappears and emission bands related to bimetallic NCs start to increase. The optimization for *protein content* showed similar results to the BSA experiments. For low LYZ content, the formation of plasmonic NPs with purple color was favorable. When LYZ excess reached the *ca.* 9-fold amount of Au, the presence of an emission band is observed. It was found that the PL intensity for LYZ_I-Au/Ag and LYZ_{II}-Au/Ag continuously increased to LYZ_I-Au/Ag 100:1.0:0.09 and LYZ_{II}-Au/Ag 126:1.0:0.03 wt ratios but at a higher ratio, the intensity started to decrease.

For *temperature* similar effect was obtained; the optimal value is 25 °C. By tuning the temperature from 40 °C to 25 °C, the PL emission maxima shifted to $\lambda_{LYZI\text{-}Au/Ag}$ = 597 nm (from 629 nm) and $\lambda_{LYZII\text{-}Au/Ag}$ 567 nm (from 598 nm), respectively.

The effect of initial *total metal content was* investigated in the range of 0.3 to 3.0 mM concentration (Fig. 2B). It was found that in both cases the lower metal contents provided better results: the application of 0.375 and 0.50 mM metal concentration resulted in the same PL intensity values so the samples with higher metal content were chosen for further studies.

As Fig. 2C represents the PL of the sample does not change significantly after 24 h, so this value was chosen as optimal reaction time.

3.2. Characterization of the bimetallic nanoclusters

3.2.1. Spectrofluorometric measurements

First, the determination of the final metal concentration in the NCs suspensions was carried out by ICP-MS. It was obtained that after purification, the suspensions contain ca. 65 % and 80 % of the initial Au- and Ag-content, respectively (**Table S1**). As it can be seen in the previous chapter, the optimized clusters show orange-red and yellow emissions; the exact PL emission bands were slightly shifted due to the purification process. Namely, the BSA-Au/Ag NCs show an intensive emission band at 620 nm (λ_{ex} = 365 nm, Fig. S1A). Using 370 nm as excitation wavelength, characteristic fluorescence can be identified at 600 and 570 nm in the case of LYZ_I- and LYZ_{II}-Au/Ag NCs, respectively (Fig. S2B and S2C). The absolute internal quantum yield (QY) values of the NCs were also calculated. As Table 1 summarizes, the presence of a small silver amount in the cluster cores can cause a dominant increase in the QY. Namely, ca. QY = 1.5 % internal quantum efficiency is measured for the monometallic NCs, while the bimetallic NCs show ca. 2.5, 7.5, and 4.8 % utilization of the excitation light in the case of BSA-Au/Ag, LYZ_I- and LYZ_{II}-Au/Ag NCs, respectively. It was clearly confirmed that a small amount of Ag can cause even a 7.5-fold enhancement of the QY depending on the type of stabilizing protein.

Moreover, the typical decay profiles were also registered (Fig. 3A and S2). In the case of every sample, three dominant components (Fig. 3B) were calculated. Their values and ratios clearly show the exact origin of the fluorescence [35].

As Table 2 shows, the most dominant components are the longest τ_2, which contributes>80–90 % to the total fluorescence signal. Besides, all NCs have an ultra-short component (τ_3) at ca. 1.5 ns, which belongs to the metal-centered emission. The similitude of the values clearly proves the almost same chemical structure of the metal cores. In contrast, the most dominant longer τ_1 of BSA- or LYZ_I-Au/Ag NCs, as well as the τ_2 of LYZ_{II} NCs, can be identified as ligand-centered emission. The ultra-long microsecond-ranged components of the orange-emitting NCs refer to the strong $n \rightarrow \pi^*$ interactions between the adjacent C=O groups in the ligand. The τ_1 component of the LYZ_{II}-Au/Ag NCs reveals the presence of the ligand-to-metal–metal charge transfer over a fluorescence period.

3.2.2. XPS, CD, and FT-IR studies

To prove the reduction of the metal ions as well as the formation of sub-nanometer sized NCs the binding energies of the metal atoms in NCs were analyzed by XPS. Since the silver content in the lyophilized samples did not reach the detection limit of the technique, data for only gold is presented. Binding energies summarized in Table 1 decisively confirm the metallic property of the gold [36–38], because the Au $4f_{7/2}$ energies are varied between 83.7 and 84.5 eV, while the Au $4f_{5/2}$ energies appear in the range of 87.4–88.2 eV.

The results of CD studies are summarized in Fig. 4. It is generally concluded that the formation of the ultra-small metal cores facilitates the stretching of the protein chains, which is supported by the ratios of secondary structure elements before and after the synthesis.

For BSA-containing systems, it is clearly observable that the α-helix content drastically decreases from 51.7 % to 12.9 %, while the ratio of the random coil sequences significantly increases from 15 % to 45 % (data in **Table S2**). In contrast, the formation of metal cores could slightly rearrange the conformation of the protein chains in the case of LYZ-stabilized systems. Although, the amount of the α-helix sequences also decreased, the β-elements (such as sheets and turns) became more dominant. The results of the FT-IR show nearly the same tendency as CD supported. The detailed data are presented on **Figure S3**.

3.3. Interaction of bimetallic NCs with Chit/HyA biocolloids

3.3.1. DLS studies

*Fig. 5. represents the change of the size (Z-average) of the labeled core–shell type carrier particles as a function of m_{NC}:$m_{carrier}$.

The samples showed very high stability in solution with both types of Au/Ag NCs, as a relatively high amount of NC could not aggregate the biocolloids (Fig. 5 **B,D**). This is a major difference compared to BSA- and LYZ-Au NCs, where the systems easily aggregated at relatively low m_{NC}:$m_{carrier}$ ratios (<0.2) (Fig. 5A,C). At high ratios, where the amount of NCs is higher than the nanocarriers, the systems remain stable, but sedimented particles could be detected in the bottom of the samples. For Type III with 40:1 Chit:HyA mass ratio (Fig. 5A,B), the particle size slowly increases to *ca.* 700–750 nm for BSA-stabilized Au/Ag NCs above m_{NC}:$m_{carrier}$ > 2.0 (Fig. 5B), while for LYZ_I-Au/Ag NCs the particle size is less than ~ 400 nm. Only minimal sedimentation could be detected. In the case of Type III with 10:1 ratio (Fig. 5C, D), the formation of aggregated particles occurs from m_{NC}:$m_{carrier}$ > 1.5, and compared to Type III with 40:1 ratio larger aggregates were formed (d > 1000 nm) (Fig. 5D). Particle stability was checked by zeta potential measurements as well. In almost all cases, the values showed high stability (~ +20 mV in buffer and ~ +60 mV in water), and this value only decreased when the aggregates were present in the samples. For Type II particles the DLS studies showed similar trends as it was observed for Type III 40:1 samples (Fig. 5A,B). Namely, the average particle diameter is highly increased above 0.07 and 0.15 m_{NC}:$m_{carrier}$ for BSA-Au NCs and LYZ-AuNCs, respectively. For alloy NCs, ~ 250 nm average diameter was measured to m_{NC}:$m_{carrier}$ ~ 3.0 (for BSA-based Au/Ag NCs) and ~ 2.0 (for LYZ-based Au/Ag NCs). The measured zeta potentials showed similar

Table 1
The w% of the metals in the final product, the excitation (λ_{ex}) and emission (λ_{em}) wavelengths, the internal quantum yields (QY), and the binding energies of the Au 4f electrons defined by XPS in cluster cores of the protein-Au/Ag NCs.

Type of NCs	w% of the metals	λ_{ex} (nm)	λ_{em} (nm)	QY (%)	Au $4f_{7/2}$ (eV)	Au $4f_{5/2}$ (eV)
BSA-Au	$Au_{100\%}$	350	660	1.47 ± 0.41	88.2	84.5
LYZ-Au	$Au_{100\%}$	350	645	1.54 ± 0.43	87.4	83.7
BSA-Au/Ag	$Au_{93}Ag_7$	365	620	2.47 ± 0.61	87.8	84.1
LYZ_I-Au/Ag	$Au_{90}Ag_{10}$	370	600	7.44 ± 0.59	87.8	84.1
LYZ_{II}-Au/Ag	$Au_{96}Ag_4$	370	570	4.78 ± 0.34	87.9	84.2

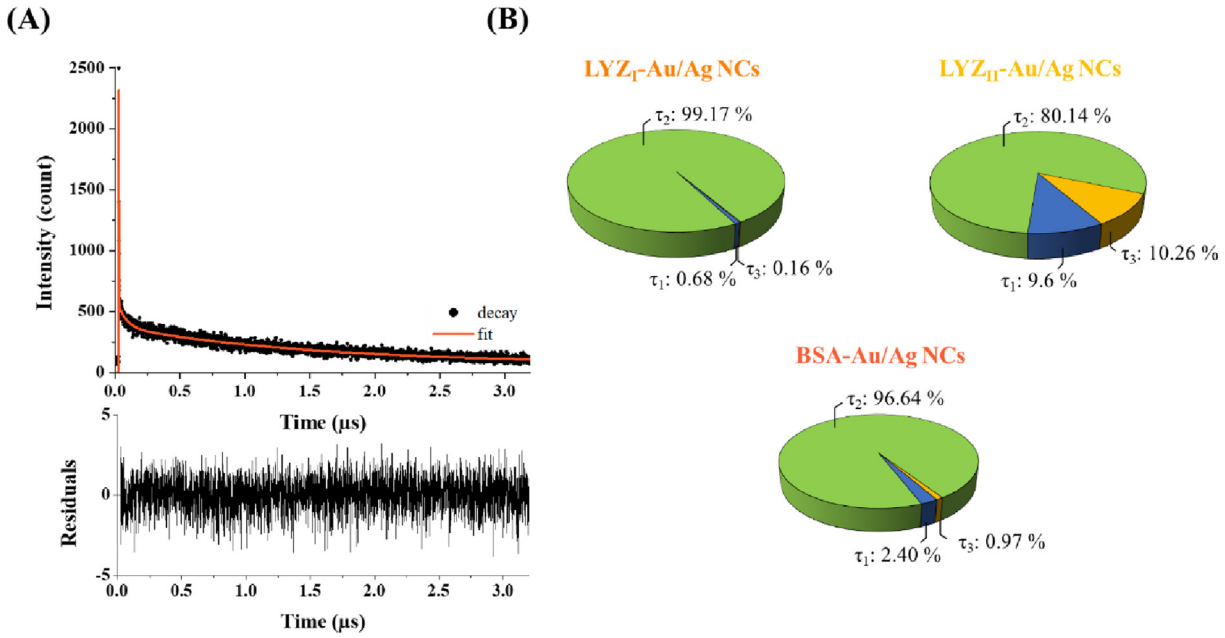

Fig. 3. The typical fluorescence decay profiles with the fitting of **(A)** BSA-Au/Ag NCs and (**B**) the ratios of the determined three dominant lifetime components in the case of BSA-, LYZ_I-, and LYZ_{II}-Au/Ag NCs.

Table 2
The determined lifetime values (τ) with the χ^2, which refers to the goodness of the fittings.

Type of NCs	τ_1 (ns)	τ_2 (μs)	τ_3 (ns)	χ^2
BSA-Au/Ag	63.8 ± 21.7	1.53 ± 0.09	1.6 ± 0.3	1.039
LYZ_I-Au/Ag	178.5 ± 70.7	5.83 ± 1.24	1.5 ± 0.2	1.081
LYZ_{II}-Au/Ag	6.8 ± 0.6	0.58 ± 0.03	1.3 ± 0.2	1.156

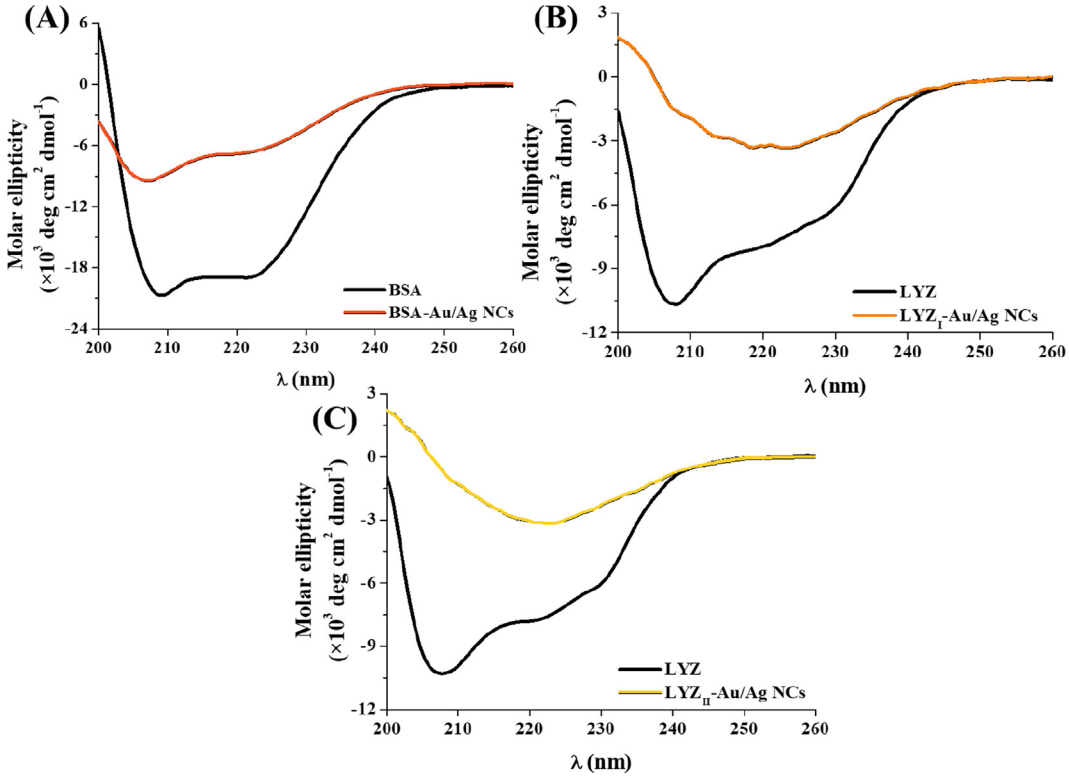

Fig. 4. The registered CD spectra of the pure proteins and **(A)** BSA-, **(B)** LYZ_I-, and **(C)** LYZ_{II}-Au/Ag NCs. ($c_{proteins}$ = 26.9 μg/mL for BSA, LYZ_I and 25.6 μg/mL for LYZ_{II}).

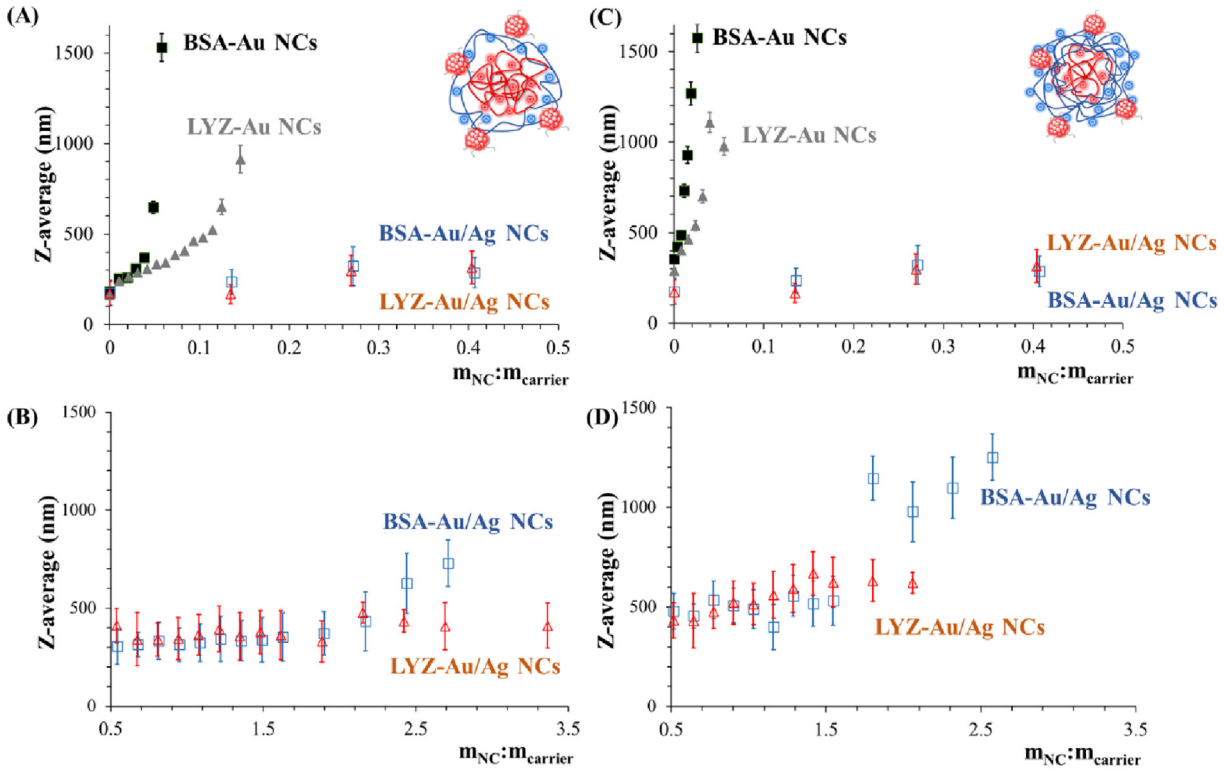

Fig. 5. Average particle size of type III (40:1 (**A, B**) and 10:1 (**C, D**) Chit:HyA ratio) colloidal NPs labeled with BSA- (■) and LYZ-(▲) pure Au (filled symbol) and BSA- (□) and LYZ-(Δ) Au/Ag (unfilled symbol) NCs as a function of m_{NC}:$m_{carrier}$.

values and change in trend as it was obtained for Type III particles. It can be concluded that the interaction of the protein-directed alloy NCs with classic alloy and core–shell type colloidal carrier particles built up from HyA and Chit polysaccharides resulted in "complex particles" having higher colloidal stability compared to the case of pure gold-based derivatives stabilized with the same proteins. When comparing the proteins, it can be stated that higher colloidal stability is observed for those containing lysozyme regardless of the quality of the noble metals.

3.3.2. Fluorimetric and fluorescent microscopy studies

Although the bimetallic NCs-biocolloid complex systems showed higher colloid stability (no aggregation) and the alloy NCs have significantly higher QY, the detected fluorescence of the labelled carrier particles-containing dispersion (Fig. 6.) is not outstanding contrary to the pure gold-containing labeled drug carriers.

While the monometallic Au NCs formed larger aggregates with the carrier particles even in small concentrations, which causes enhanced photoluminescent behavior due to the aggregation-induced emission (AIE) process, this effect is not observed for alloy derivatives. The fluorescence measurements (Fig. 6) are in good agreement with the DLS data (Fig. 5) confirming the avoidance of the aggregation and thus the lack of the AIE in the case of the studied bimetallic NCs. As Fig. 6 represents, the change of the fluorescent signal follows the shape of the diameter change curve. Any dominant and significant variations cannot be observed, the weak AIE enhancement is experienced only at the higher concentration

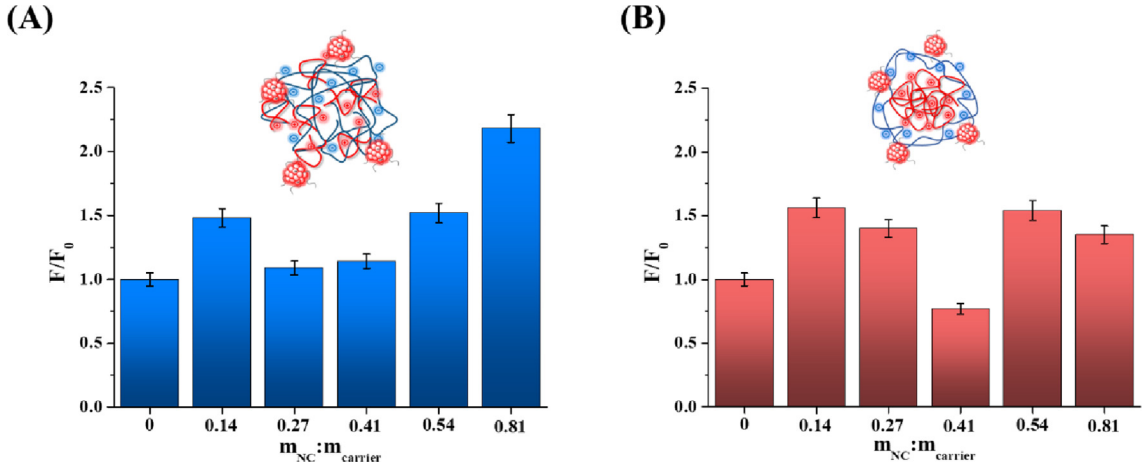

Fig. 6. The relative fluorescence intensities (F/F_0) in the case of **(A)** BSA-Au/Ag NCs + Type II carrier composite and **(B)** LYZ_I-Au/Ag NCs + Type III 40:1 complex particles.

ratios (m_{NC}:$m_{carrier}$ > 0.5) dominantly for BSA-Au/Ag NCs + Type II (Fig. 6A). The interaction of both Type II and Type III particles with BSA-stabilized mono- or bimetallic NCs results in the presence of aggregates at relatively lower m_{NC}:$m_{carrier}$, which is confirmed by the DLS studies as well. The bimetallic NCs-biocolloid complex systems were analyzed by fluorescent microscopy as well. 2 mL of sonicated sample was moved into centrifuge tubes, and then centrifugated at 12000 rpm for 10 min. The supernatant was removed and exchanged for ultrapure water, and then redispersed by shaking and sonication. The dried samples can be visualized by microscopy, as **Fig.S4.** presents. However, quantitative analysis cannot be purely deduced from microscopic images, but the effectiveness of fluorescent labelling can be established. The pure carrier particles do not PL properties as it was previously presented in our article [33], but even a small amount of bimetallic NCs show appropriate fluorescence using a red filter, and no further sample preparation was needed, as in the case of labeling with Au NCs. Based on microscopic images no further conclusions can be made.

4. Conclusion

Template-assisted one-step preparation protocols of BSA- and LYZ-stabilized fluorescent Au/Ag alloy NCs were demonstrated at room temperature for the first time. The alloying process resulted in enhanced QY and blue-shifted emission for the alloy NCs compared to the purely gold-based derivatives. The nanostructures as well as the characteristic optical features were determined in detail by several physico-chemical techniques. The optical properties (emission wavelength, quantum yield) of the nanoclusters produced by the alloying process meet the requirements of the "biological window" (λ_{em} > 600 nm) and its presumably biocompatible character may make it an optimal FRs. It was found that, in contrast to the monometallic derivatives, our bimetallic NCs, prepared at mild conditions show high stability after interaction with biocompatible, hyaluronic acid-covered drug carrier particles. However, even though our alloy NCs possess enhanced QY and higher colloidal stability than the monometallic gold NCs stabilized by same proteins, but dominant PL enhancing can not be detected on the labelled carrier particles. We have demonstrated that alloying process and the milder preparation conditions of noble metal NCs can be a promising route to the fabrication of novel nanostructures as fluorescent reporters.

CRediT authorship contribution statement

Árpád Turcsányi: Methodology, Investigation, Writing – original draft. **Ditta Ungor:** Investigation, Writing – original draft. **Marek Wojnicki:** Validation, Formal analysis, Writing – review & editing. **Edit Csapó:** Conceptualization, Visualization, Writing – original draft, Writing – review & editing, Supervision, Resources.

Data availability

Data will be made available on request.

Declaration of Competing Interest

The authors declare that they have no known competing financial interests or personal relationships that could have appeared to influence the work reported in this paper.

Acknowledgement

Project no. TKP2021-EGA-32 has been implemented with the support provided by the Ministry of Innovation and Technology of Hungary from the National Research, Development, and Innovation Fund, financed under the TKP2021-EGA funding scheme. This research was also supported by the National Research, Development, and Innovation Office through FK131446 project. The publication was also funded by the University of Szeged Open Access Fund (FundRef, Grant No. 5990).

Appendix A. Supplementary material

Supplementary data to this article can be found online at https://doi.org/10.1016/j.molliq.2022.121002.

References

[1] Ł. Lamch, A. Pucek, J. Kulbacka, M. Chudy, E. Jastrzębska, K. Tokarska, M. Bułka, Z. Brzózka, K.A. Wilk, Recent progress in the engineering of multifunctional colloidal nanoparticles for enhanced photodynamic therapy and bioimaging, Adv. Colloid Interface Sci. 261 (2018) 62–81.
[2] T. Zhou, X. Zhao, L. Liu, P. Liu, Preparation of biodegradable PEGylated pH/reduction dual-stimuli responsive nanohydrogels for controlled release of an anti-cancer drug, Nanoscale. 7 (28) (2015) 12051–12060.
[3] H. Sahoo, Fluorescent labeling techniques in biomolecules: a flashback, RSC Adv. 2 (2012) 7017–7029.
[4] S.E. Slezak, K.A. Muirhead, Radioactive cell membrane labelling, Nature. 352 (6332) (1991) 261–262.
[5] G. Lukinavičius, C. Blaukopf, E. Pershagen, A. Schena, L. Reymond, E. Derivery, M. Gonzalez-Gaitan, E. D'Este, S.W. Hell, D.W. Gerlich, K. Johnsson, SiR-Hoechst is a far-red DNA stain for live-cell nanoscopy, Nat. Commun. 6 (2015) 1–7.
[6] M. Wojnicki, V. Hessel, Quantum materials made in microfluidics - critical review and perspective, Chem. Eng. J. 438 (2022).
[7] X. Huang, I.H. El-Sayed, W. Qian, M.A. El-Sayed, Cancer cell imaging and photothermal therapy in the near-infrared region by using gold nanorods, J. Am. Chem. Soc. 128 (6) (2006) 2115–2120.
[8] Y. Zheng, L. Lai, W. Liu, H. Jiang, X. Wang, Recent advances in biomedical applications of fluorescent gold nanoclusters, Adv. Colloid Interface Sci. 242 (2017) 1–16.
[9] D. Ungor, I. Dékány, E. Csapó, Reduction of tetrachloroaurate(Iii) ions with bioligands: Role of the thiol and amine functional groups on the structure and optical features of gold nanohybrid systems, Nanomaterials. 9 (2019) 1229.
[10] G.S. Gupta, A. Kumar, V.A. Senapati, A.K. Pandey, R. Shanker, A. Dhawan, Laboratory scale microbial food chain to study bioaccumulation, biomagnification, and ecotoxicity of cadmium telluride quantum dots, Environ. Sci. Technol. 51 (3) (2017) 1695–1706.
[11] K. Sytwu, M. Vadai, J.A. Dionne, Bimetallic nanostructures: combining plasmonic and catalytic metals for photocatalysis, Adv. Phys.: X 4 (2019) 1619480.
[12] D. Ungor, K. Horváth, I. Dékány, E. Csapó, Red-emitting gold nanoclusters for rapid fluorescence sensing of tryptophan metabolites, Sens. Actua. B Chem. 288 (2019) 728–733.
[13] D. Ungor, E. Csapó, B. Kismárton, A. Juhász, I. Dékány, Nucleotide-directed syntheses of gold nanohybrid systems with structure-dependent optical features: Selective fluorescence sensing of Fe3+ ions, Colloids Surfaces B Biointerfaces. 155 (2017) 135–141.
[14] E. Csapó, D. Ungor, Á. Juhász, G.K. Tóth, I. Dékány, Gold nanohybrid systems with tunable fluorescent feature: Interaction of cysteine and cysteine-containing peptides with gold in two- and three-dimensional systems, Colloids Surf. A Physicochem. Eng. Asp. 511 (2016) 264–271.
[15] E. Csapó, D. Ungor, Z. Kele, P. Baranyai, A. Deák, Á. Juhász, L. Janovák, I. Dékány, Influence of pH and aurate/amino acid ratios on the tuneable optical features of gold nanoparticles and nanoclusters, Colloids Surf. A Physicochem. Eng. Asp. 532 (2017) 601–608.
[16] H. Chen, L. Lin, H. Li, J. Li, J.-M. Lin, Aggregation-induced structure transition of protein-stabilized zinc/copper nanoclusters for amplified chemiluminescence, ACS Nano. 9 (2) (2015) 2173–2183.
[17] E.A. Ivleva, E.A. Obraztsova, E.R. Pavlova, O.V. Morozova, D.G. Ivanov, A.S. Kononikhin, D.V. Klinov, Albumin-stabilized fluorescent metal nanoclusters: fabrication, physico-chemical properties and cytotoxicity, Mater. Des. 192 (2020).
[18] N. Pajooheshpour, M. Rezaei, A. Hajian, A. Afkhami, M. Sillanpää, F. Arduini, H. Bagheri, Protein templated Au-Pt nanoclusters-graphene nanoribbons as a high performance sensing layer for the electrochemical determination of diazinon, Sens. Actu. B Chem. 275 (2018) 180–189.
[19] N. Zhang, Y. Si, Z. Sun, L. Chen, R. Li, Y. Qiao, H. Wang, Rapid, selective, and ultrasensitive fluorimetric analysis of mercury and copper levels in blood using bimetallic gold-silver nanoclusters with "silver effect"-enhanced red fluorescence, Anal. Chem. 86 (23) (2014) 11714–11721.
[20] S. Bhunia, S. Kumar, P. Purkayastha, Dependence of ultrafast dynamics in gold–silver alloy nanoclusters on the proportion of the metal content, SN Appl. Sci. 1 (2019) 1–11.
[21] J.S. Mohanty, P.L. Xavier, K. Chaudhari, M.S. Bootharaju, N. Goswami, S.K. Pal, T. Pradeep, Luminescent, bimetallic AuAg alloy quantum clusters in protein templates, Nanoscale. 4 (2012) 4255–4262.

[22] T. Feng, Y. Chen, B. Feng, J. Yan, J. Di, Fluorescence red-shift of gold-silver nanoclusters upon interaction with cysteine and its application, Spectrochim. Acta - Part A Mol. Biomol. Spectrosc. 206 (2019) 97–103.
[23] Z. Chu, L. Chen, X. Wang, Q. Yang, Q. Zhao, C. Huang, et al., Ultrasmall Au-Ag Alloy nanoparticles: protein-directed synthesis, biocompatibility, and X-ray computed tomography imaging, ACS Biomater. Sci. Eng. 5 (2019) 1005–1015.
[24] R. Dai, W. Deng, P. Hu, C. You, L. Yang, X. Jiang, X. Xiong, K. Huang, One-pot synthesis of bovine serum albumin protected gold/silver bimetallic nanoclusters for ratiometric and visual detection of mercury, Microchem. J. 139 (2018) 1–8.
[25] H. Sun, T. Qing, X. He, J. Shangguan, R. Jia, H. Bu, J. Huang, K. Wang, Rapid synthesis of Au/Ag bimetallic nanoclusters with highly biochemical stability and its applications for temperature and ratiometric pH sensing, Anal. Chim. Acta. 1070 (2019) 88–96.
[26] H. Liu, X. Zhang, X. Wu, L. Jiang, C. Burda, J.J. Zhu, Rapid sonochemical synthesis of highly luminescent non-toxic AuNCs and Au@AgNCs and Cu (ii) sensing, Chem. Commun. 47 (2011) 4237–4239.
[27] W. Mi, S. Tang, Y. Jin, N.a. Shao, Au/Ag bimetallic nanoclusters stabilized by glutathione and lysozyme for ratiometric sensing of H2O2and Hydroxyl Radicals, ACS Appl. Nano Mater. 4 (2) (2021) 1586–1595.
[28] S. Borse, Z.V.P. Murthy, T.-J. Park, S.K. Kailasa, Lysozyme-decorated gold and molybdenum bimetallic nanoclusters for the selective detection of bilirubin as a jaundice biomarker, ACS Appl. Nano Mater. 4 (11) (2021) 11949–11959.
[29] V. Hornok, E. Csapó, N. Varga, D. Ungor, D. Sebők, L. Janovák, G. Laczkó, I. Dékány, Controlled syntheses and structural characterization of plasmonic and red-emitting gold/lysozyme nanohybrid dispersions, Colloid Polym. Sci. 294 (1) (2016) 49–58.
[30] A. Czyżowska, A. Barbasz, L. Szyk-Warszyńska, M. Oćwieja, E. Csapó, D. Ungor, The surface-dependent biological effect of protein-gold nanoclusters on human immune system mimetic cells, Colloids Surf. A Physicochem. Eng. Asp. 620 (2021).
[31] D. Ungor, A. Barbasz, A. Czyżowska, E. Csapó, M. Oćwieja, Cytotoxicity studies of protein-stabilized fluorescent gold nanoclusters on human lymphocytes, Colloids Surf. B Biointerfaces. 200 (2021).
[32] Á. Turcsányi, N. Varga, E. Csapó, Chitosan-modified hyaluronic acid-based nanosized drug carriers, Int. J. Biol. Macromol. 148 (2020) 218–225.
[33] Á. Turcsányi, D. Ungor, E. Csapó, Fluorescent labeling of hyaluronic acid-chitosan nanocarriers by protein-stabilized gold nanoclusters, Cryst. 10 (2020) 1113.
[34] J. Reed, T.A. Reed, A set of constructed type spectra for the practical estimation of peptide secondary structure from circular dichroism, Anal. Biochem. 254 (1) (1997) 36–40.
[35] T.Q. Yang, B. Peng, B.Q. Shan, Y.X. Zong, J.G. Jiang, P. Wu, K. Zhang, Origin of the photoluminescence of metal nanoclusters: from metal-centered emission to ligand-centered emission, Nanomaterials. 10 (2020) 261.
[36] S. Peters, S. Peredkov, M. Neeb, W. Eberhardt, M. Al-Hada, Size-dependent XPS spectra of small supported Au-clusters, Surf. Sci. 608 (2013) 129–134.
[37] M.P. Casaletto, A. Longo, A. Martorana, A. Prestianni, A.M. Venezia, XPS study of supported gold catalysts: the role of Au0 and Au+δ species as active sites, Surf. Interface Anal. 38 (2006) 215–218.
[38] C. Battistoni, G. Mattogno, F. Cariati, L. Naldini, A. Sgamellotti, XPS photoelectron spectra of cluster compounds of gold, Inorganica Chim. Acta. 24 (1977) 207–210.